A Machine Learning-Based Surrogate Modeling Framework for Predicting the History-Dependent Deformation of Dual Phase Microstructures

Sarthak Khandelwal
Department of Metallurgical Engineering and Materials Science
Indian Institute of Technology Bombay
Mumbai, India - 400076
sarthak.k@iitb.ac.in

Soudip Basu
Department of Metallurgical Engineering and Materials Science
Indian Institute of Technology Bombay
Mumbai, India - 400076
soudipbasu.1992@gmail.com

Anirban Patra *
Department of Metallurgical Engineering and Materials Science
Indian Institute of Technology Bombay
Mumbai, India - 400076
anirbanpatra@iitb.ac.in
(* Corresponding author)

October 14, 2021

ABSTRACT

A Machine Learning (ML)-based surrogate modeling framework is developed to predict the heterogeneous deformation behavior of dual phase microstructures. The deformation is first simulated using a dislocation density-based J2 plasticity Finite Element (FE) model, whose results form the basis for surrogate model training and validation. Long Short Term Memory (LSTM)-based ML models, with different architectures, are employed to predict the spatio-temporal evolution of three output variables: effective strain, von Mises effective stress, and the stress triaxiality ratio. Two metrics, the mean average error (MAE) and the coefficient of determination, R^2, are used to assess the performance of the models and different architectures. Based on our analysis, the LSTM model is generally found to predict the spatio-temporal deformation fields with reasonable accuracy, even for untrained microstructures with varying microstructural attributes and random instantiations. The LSTM model is also used to predict aggregate properties, such as the stress-strain response and the strain partitioning in the dual phase microstructures.

*K*eywords Surrogate models · Machine Learning (ML) · Long-Short Term Memory (LSTM) · dual phase microstructures · plastic deformation

1 Introduction

Finite Element (FE) modeling frameworks have been used extensively to simulate the spatio-temporal deformation (and evolution) of microstructures. Such frameworks are based on the development of constitutive equations to represent the underlying deformation mechanisms. These frameworks have generally been developed, with various homogenization

approaches (if required), to study the deformation at the level of components [1, 2], microstructures [3, 4], and nano-scale structures [5, 6, 7]. The FE frameworks often employ physically-representative Crystal Plasticity (CP) constitutive equations [3, 8, 9] and phase field modeling approaches [10, 11, 12, 13] to study the microstructure evolution during deformation and correlate them with the overall mechanical response. Additionally, Fast-Fourier Transform (FFT) based spectral solvers [14, 15, 16] have also been developed to study the deformation of microstructure ensembles. These predictions are also compared with relevant experimental measurements [17, 18, 4], where available. These spatially resolved deformation simulations are generally considered to be the state-of-the-art and provide high fidelity information regarding local deformation characteristics. They have become the tool of choice for studying the effect of microstructure on the deformation behavior. However, these methods are associated with large computational costs, which may act as a deterrent for performing large scale simulations for advanced computational materials design problems.

In recent years, surrogate modeling techniques are being explored as an alternative can significantly reduce the computational times, while maintaining the high fidelity of microstructural information obtained from FE simulations. These approaches generally employ a combination of data informatics, image-based modeling and neural networks to predict microstructure evolution during deformation [19, 20, 21]. This is accomplished by training the surrogate models to the spatio-temporal data obtained from FE or FFT simulations [22, 23, 24, 25, 26, 27, 28]. In some cases, the FE simulations may even be bypassed by directly training the surrogate models to the experimentally obtained microstructure evolution data [29]. Further, surrogate constitutive model forms have also been trained using data-based approaches to the "original" model response [30, 31, 32] and implemented in FE frameworks to obtain reduced computation times [31, 33]. Such surrogate models broadly fall in the domain of machine learning techniques.

Machine Learning (ML) is an emerging research field and has been widely adopted in recent years due to its ability to predict properties, relationships and inferences from different kinds of data, with relatively lower computational costs [34]. While research in this field has increased significantly in the recent years [35], we mention a few examples of the application of ML techniques specific to mechanics and microstructure evolution problems in the following (this being the central theme of our work). Mangal and Holm [25] used ML to predict the formation of stress hot spots in face centered cubic materials. They implemented a random forest algorithm, which was used for classification of grains as stress hot spots, where localized deformation may occur. The algorithm also successfully captured the effect of changing material and texture parameters on the stress hot spots. Muhammad et al. [29] implemented an Artificial Neural Network (ANN) model to predict the local strain distribution, fracture, and evolution of plastic anisotropy in additively manufactured alloys. They were able to predict the location, intensity and the shape of shear bands before failure with reasonable accuracy. An image-based Convolutional Neural Network (CNN) model was developed by Beniwal et al. [21] for predictive modeling of structure-property linkages. In their work, the reduced order model has the ability to predict stress localization simply from the microstructure image. Machine learning was also used to homogenize arbitrary microstructures and obtain the corresponding nonlinear, history-dependent constitutive response [33]. A Long-Short Term Memory (LSTM) based RNN network has the capability of remembering states over time and thus capable of modeling dynamic systems [36]. Pandey et al. [27] developed a LSTM-based framework for predicting the texture evolution under tensile loading of polycrystalline materials. They used a first-order approximation by taking the effect of only nearest neighbor interactions on each material point. Although their model did not account for any long range interactions, it produced results with 99% accuracy. Moreover, the prediction capability of their model for different microstructures was not explored exhaustively. Several other ML-based studies for predicting deformation have been published in the recent years [37, 38, 39, 40, 41].

Most of the above mentioned surrogate modeling studies generally focused on predicting the deformation of single phase microstructures. Multi-phase microstructures are generally associated with heterogeneous deformation characteristics and partitioning of stress and strain in different regions of the microstructure [17]. This poses a challenge for ML-based surrogate modeling approaches, as the evolution stress and strain distributions is not only history-dependent, but also dependent on the spatial heterogeneity of the underlying microstructures. Further, while some studies have indeed developed ML models for multi-phase microstructures [21, 42], their predictive capabilities as a function of deformation history has not been clearly demonstrated; majority of the studies are only used predict the contours at the end of deformation.

In the present work, we focus on predicting the history-dependent microstructure evolution of dual phase microstructures during deformation using surrogate ML models. Dual phase microstructures, comprising of a hard martensite phase and a soft ferrite phase (representative of the martensite and ferrite phases, respectively), are first simulated using a dislocation density-based, J2 plasticity FE model. The output from the FE model is used to generate the data set for surrogate model training and also serves as the ground truth data. A systematic study of different LSTM-based surrogate models, and trained with the same FE data set, is performed for predicting the deformed microstructure evolution. Specifically, effective strain, von Mises effective stress, and Stress Triaxiality ratio (ST) are chosen as the

output variables of the models. The model with the least error in predictions is then used for predicting the spatial deformation contours, aggregate stress-strain response as well the strain partitioning for untrained microstructures.

2 Finite Element (FE) Framework and Data Set Generation

2.1 Microstructure Instantiation

We have used an in-house MATLAB code to instantiate 2D dual phase microstructures. This code employs a weighted Voronoi tessellation algorithm for random positioning of grain centers within the simulation domain, based on pre-assigned grain size distributions. This algorithm randomly instantiates grain seed locations, such that the projected grain radii do not overlap. The grain interfaces are then defined based on the proximity of a point to a grain seed, thus assigning points in the simulation domain to different grains. Details of the microstructure instantiation algorithm are given in Ref. [43]. The grain size distributions and phase fractions of the respective phases used in this work are based on experimental characterization of a Dual Phase (DP) steel microstructure, comprised of soft ferrite and hard martensite phases. A log normal grain size distribution has been assumed for both phases. Figure 1 shows the phase map and the grain map of a representative microstructure generated using this algorithm. The Trelis meshing software [44] is then used to mesh the 2D microstructure with voxel-based finite elements. An element size of $0.25\mu m$ is used to mesh the simulation domain of $100 \times 100\mu m^2$.
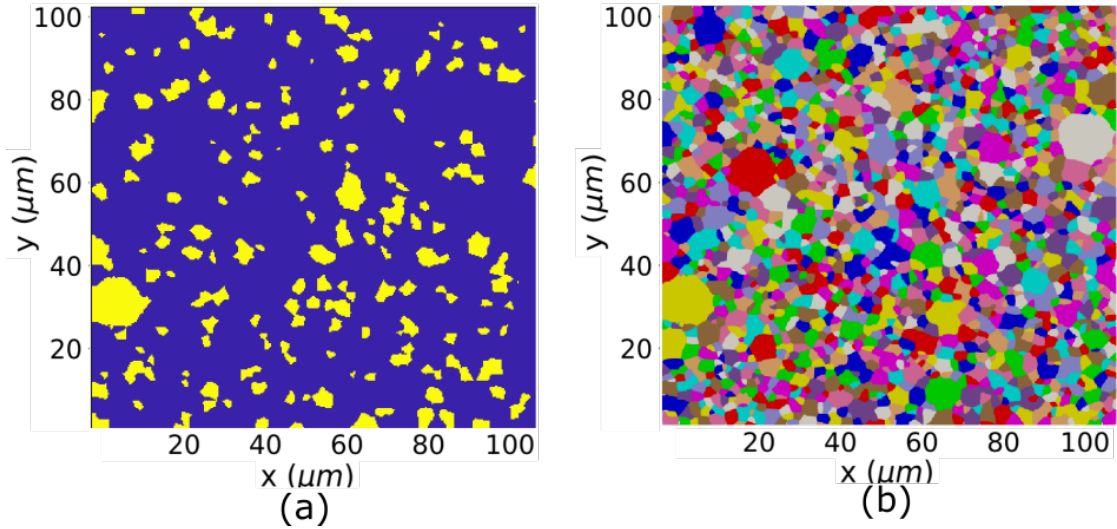

Figure 1: (a) Phase map, and (b) grain map of a representative dual phase microstructure. In the phase map, blue color corresponds to the ferrite phase with higher volume fraction, while yellow color corresponds to the martensite phase with lower volume fraction. Note that the colors in the grain map are random and only used to demarcate one grain from another.

2.2 Constitutive Model

We have used a J2 plasticity constitutive modeling framework [45] for performing the Finite Element (FE) simulations. While this is not a novel feature of the present work, we briefly mention the constitutive equations here for completeness. Detailed description of the constitutive model developed for Dual Phase (DP) steels and analysis of the model results are given elsewhere [46]. This constitutive framework uses a finite deformation, dislocation density based model and has been adapted from a crystal plasticity framework, previously used to model the deformation behavior of various metallic systems [18, 4, 47].

In this framework, the deformation gradient is multiplicatively decomposed into the elastic and plastic parts:

$$\boldsymbol{F} = \boldsymbol{F^e} \cdot \boldsymbol{F^p} \tag{1}$$

where, $\boldsymbol{F^p}$ relates the reference configuration to an intermediate configuration and accounts for shear due to plastic deformation, while $\boldsymbol{F^e}$ relates the intermediate configuration to the current, deformed deformation and accounts for the elastic deformation and rigid body rotation.

The plastic deformation gradient is related to the velocity gradient as: $\dot{\boldsymbol{F}}^{\boldsymbol{p}} = \boldsymbol{L}^{\boldsymbol{p}} \cdot \boldsymbol{F}^{\boldsymbol{p}}$, where the velocity gradient, $\boldsymbol{L}^{\boldsymbol{p}}$, is given by:

$$\boldsymbol{L}^{\boldsymbol{p}} = \sqrt{\frac{3}{2}} \dot{\bar{\epsilon}}^p \boldsymbol{N}^{\boldsymbol{p}} \tag{2}$$

Here, $\dot{\bar{\epsilon}}^p$ is the effective plastic strain rate and $\boldsymbol{N}^{\boldsymbol{p}}$ is the direction of the plastic flow, based on the following relation:

$$\boldsymbol{N}^{\boldsymbol{p}} = \sqrt{\frac{3}{2}} \frac{\boldsymbol{S}}{\bar{\sigma}} \tag{3}$$

where, $\boldsymbol{S}$ is the deviatoric stress tensor and $\bar{\sigma}$ is the von Mises effective stress. The effective plastic strain rate is modeled using a Kocks-type, thermally activated flow rule [48]:

$$\dot{\bar{\epsilon}}^p = \dot{\bar{\epsilon}}_o^p \exp\left(\frac{-\Delta F_g}{kT}\left(1 - \left(\frac{\bar{\sigma} - S_a}{S_t}\right)^p\right)^q\right) ; \bar{\sigma} > S_a \tag{4}$$

where, ΔF_g is the activation energy for dislocation glide, S_a is the athermal slip resistance, S_t is the thermal slip resistance, and p and q are parameters used to model the shape of the activation enthalpy curve. The athermal slip resistance, S_a, is given by:

$$S_a = \frac{h_p}{\sqrt{d}} + Gb\sqrt{q_p\rho} \tag{5}$$

where, h_p is the Hall-Petch hardening constant, d is the grain size, G is the shear modulus, b is the Burgers vector, q_p is the dislocation barrier strength and ρ is the total dislocation density. The thermal slip resistance S_t is given by

$$S_t = \tau_0 + \delta\tau \tag{6}$$

where, τ_0 accounts for the solute solution strengthening and lattice slip resistance while $\delta\tau$ is the strengthening due to carbon atoms in solution and carbide precipitation in martensite. These contributions are expressed as [1]:

$$tau_0 = 77 + 80\%Mn + 750\%P + 60\%Si + 80\%Cu + 45\%Ni + 60\%Cr + 11\% \tag{7}$$

$$\delta\tau = 3065\%C - 161MPa \tag{8}$$

The elemental concentrations in weight percent are taken from [2] or both phases, whereas %C for ferrite and martensite is obtained from the phase diagram as 0.056% and 0.378% respectively. The values of these parameters are given in [49]. Martensitic structures are known to derive their strength from multiple factors like boundary strengthening (martensite colony size) , solute solution strengthening, dislocation strengthening, Hall-Petch strengthening and carbide strengthening [7]. Ferrite on the other primarily undergoes dislocation, solute and Hall-Petch strengthening. These common strengthening mechanisms are appropriately accounted for through equations (6) and (7) for both the phases. Equation (8) represents strengthening due to carbon in solution for ferrite, while for martensite it additionally includes carbide precipitation. ρ is defined as the sum of mobile, ρ_M, and immobile, ρ_I, dislocation densities, i.e.,

$$\rho = \rho_M + \rho_I \tag{9}$$

Note that the FE model keeps track of the individual grain sizes, which contribute to grain size-dependent heterogeneous deformation, in addition to the heterogeneity due to the two phases.

The evolution of the dislocation densities depends on the equivalent plastic strain rate as [4, 45]:

$$\dot{\rho_M} = \frac{k_{mul}}{b}\sqrt{\rho}|\dot{\bar{\epsilon}}^p| - \frac{2R_c}{b}\rho_M|\dot{\bar{\epsilon}}^p| - \frac{1}{b\lambda}|\dot{\bar{\epsilon}}^p| \tag{10}$$

$$\dot{\rho_I} = \frac{1}{b\lambda}|\dot{\bar{\epsilon}}^p| - k_{dyn}\rho_I|\dot{\bar{\epsilon}}^p| \tag{11}$$

where, k_{mul} is the dislocation multiplication rate constant, R_c is the critical capture radius, $\lambda = \frac{1}{\beta\sqrt{\rho}}$ is effective mean free path of dislocations, and β is a constant associated with dislocation trapping. The first term in equation (10) represents the multiplication of mobile dislocations at existing dislocations, while the second term represents the mutual annihilation of dislocation dipoles, and the third term represents the trapping of mobile dislocations at barriers. k_{dyn} is the material constant associated with dynamic recovery of immobile dislocations due to thermally activated processes. The first term in equation (11) represents the rate at which mobile dislocations are trapped in barriers and become immobile, while the second term represents the rate at which the immobile dislocations are annihilated due to dynamic recovery.

The constitutive model has been implemented as a user-defined material model and interfaced with the open source finite element code, MOOSE [50]. Further details of the constitutive model, along with model parameters, are presented elsewhere [46].

2.3 Loading and Boundary Conditions

A mesh size of $0.25\mu m$ is used with a simulation domain size of $100 \times 100\mu m^2$. The simulation domain has 160,000 finite elements, with linear interpolation. A generalized plane strain assumption has been used in these essentially 2D simulations. The bottom face of the simulation domain is constrained in the y-direction, while the left face is constrained in the x-direction to resemble an axisymmetric model. The bottom left corner node, is fully constrained to prevent rigid body motion. Displacement-controlled tensile loading is applied on the right face along the positive x-direction at a nominal strain rate of $5 \times 10^{-3}s^{-1}$.

2.4 FE Model Results

Representative FE simulated contours of the effective strain, $\bar{\epsilon}$, effective stress, $\bar{\sigma}$, and Stress Triaxiality ratio (ST) after a nominal strain of 0.15 are shown in figure 2 (a), (b), and (c), respectively. The corresponding simulated stress-strain response is shown in figure 2 (d). It can be seen that the majority of the strain is localized in the softer ferrite phase (with higher volume fraction), while the stress is localized in the hard martensite phase (with lower volume fraction). On the other hand, the stresses are significantly higher in the hard martensite phase. These regions may be interpreted, with the help of the phase map (in figure 1(a)), in the corresponding effective strain and effective stress contours. As is evident, highly heterogeneous and partitioned deformation fields develop in the microstructure. The ST contour shows that there are regions of very high stress triaxiality ratio (up to 3) in the vicinity of the hard martensite phases. Specifically, the triaxiality hot spots are more predominant when two grains of the hard martensite phase are in vicinity of each other. These regions may be expected to be failure initiation points in the microstructure. This is discussed in more detail in section 4.5.

2.5 Data Extraction from FE Results

The simulation results of the FE model are output to an EXODUS data file [51]. We have used the Python-based Sandia Engineering Analysis Code Access System (SEACAS) package [52] to extract data from the binary Exodus file to an ASCII-based csv file, which are then used as inputs for the ML models. The overall integration of the FE framework with the ML-based surrogate model via the SEACAS Exodus Python library is shown schematically in Figure 3. Details of the surrogate modeling framework are described next.

3 Machine Learning (ML)-based Surrogate Modeling Framework

3.1 Long Short-Term Memory (LSTM) Network

Long Short-Term Memory (LSTM) networks are a class of Recurrent Neural Networks (RNN). LSTMs were proposed by Hochreiter and Schmidhuber [36] with the purpose of transmitting useful information multiple time steps into the future. The LSTM architecture consists of memory cells, which are recurrently connected sub-nets. The memory cell functions with the help of three gates: (a) keep gate, (b) write gate, and (c) output gate.

The memory cells have a keep gate that determines the amount of the previous memory that is useful and will be stored for future use. Once the LSTM knows which information is useful, the information is written into the memory state by the write gate. At the final step, the LSTM unit provides it's output. The structure of the output gate is similar to the write gate. All these gates use a combination of different activation functions to perform their respective tasks [53, 54]. The key equations involved in LSTM are summarized in the following [55].

$$i_t = \sigma \left(W_{xi}x_t + W_{hi}h_{t-1} + W_{ci} \odot c_{t-1} + b_i \right) \tag{12}$$

$$k_t = \sigma \left(W_{xk}x_t + W_{hk}h_{t-1} + W_{ck} \odot c_{t-1} + b_k \right) \tag{13}$$

$$c_t = k_t \odot c_{t-1} + f \left(W_{xc}x_t + W_{hc}h_{t-1} + b_c \right) \tag{14}$$

$$o_t = \sigma \left(W_{xo}x_t + W_{ho}h_{t-1} + W_{co} \odot c_{t-1} + b_o \right) \tag{15}$$

$$h_t = o_t \odot f(c_t) \tag{16}$$

Here, x_t, c_t and h_t are the input, the memory cell and the output status of the LSTM at time t, respectively. Further, i_t, o_t and k_t are the functional values of the input, output, and keep gates, respectively. W_{xj} denotes the weight matrix between the input, x_t, and the gate, j_t. Note that in the denotation for matrix W_{xj}, x and j do not represent the shape of
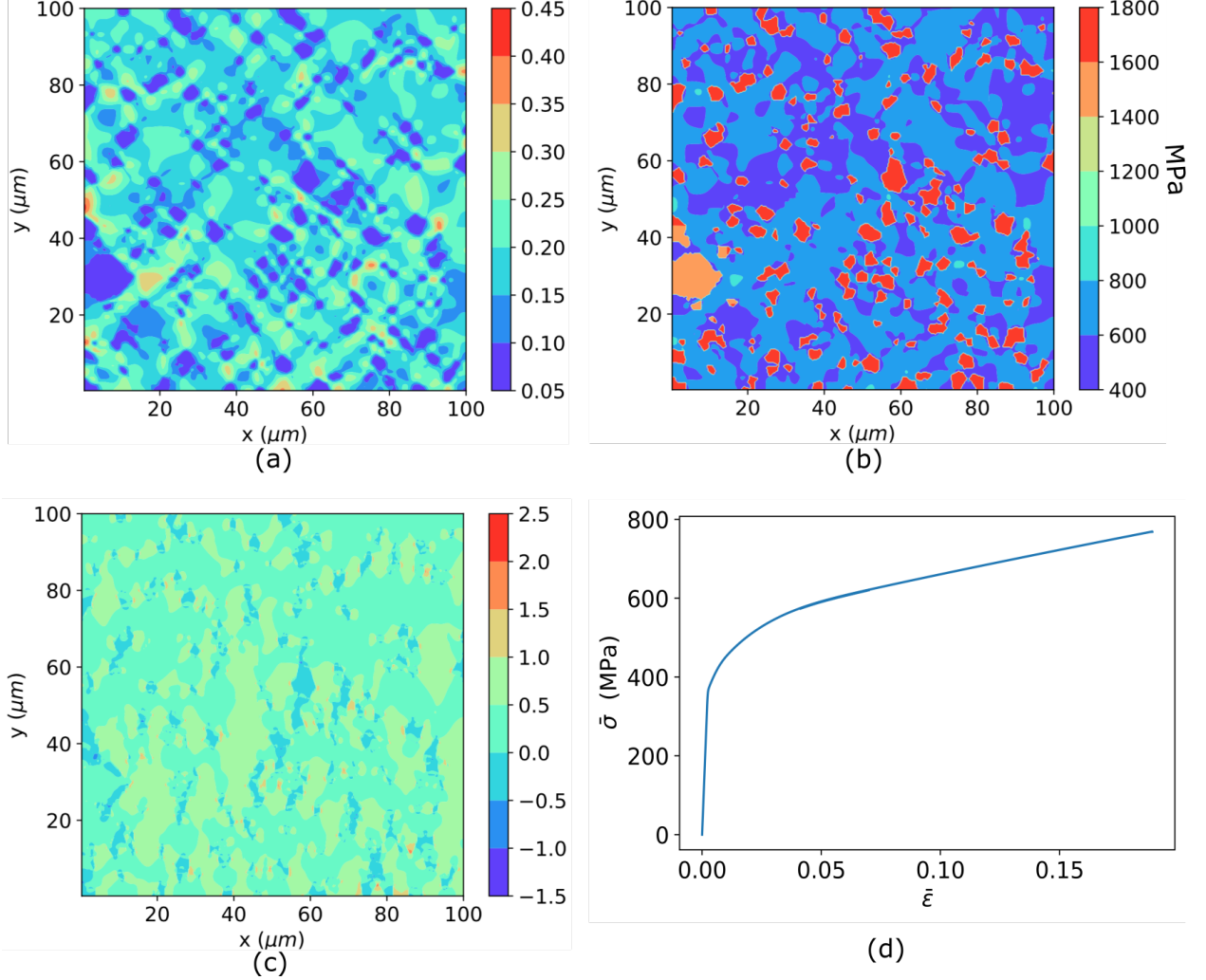
Figure 2: FE contours of (a) effective strain, (b) von Mises effective stress, and (c) Stress Triaxiality ratio (ST) after a nominal strain of 0.15. (d) Stress-strain response as obtained from FE simulations.

the matrix, but represent the input, x_t, and the gate, j_t at time t . The shape of the matrix will depend on the size of the vector x_t and nodes in the gate j_t. and b_j represents the corresponding bias. $\odot$ represents the element-wise Hadamard product. f is the activation function for the LSTM unit. The Rectified Linear activation Unit (ReLU) (equation (17)) has been used in our LSTM model. This is given by:

$$f(z) = max(0, z) \tag{17}$$

The training process is similar to that of a feed forward neural network, such as an Artificial Neural Network (ANN). A Back-Propagation Through Time (BPTT) algorithm is employed here to find optimal values of all the weights. The BPTT algorithm relies on the unrolling of the network, in which a copy is generated for each time increment, thus allowing to use a traditional back-propagation algorithm on the unrolled network [56]. The prediction accuracy of the model is studied in terms of the Mean Square Error (MSE), i.e.,

$$C = \frac{\sum_{m=1}^{n} \|\boldsymbol{y_m} - \hat{\boldsymbol{y_m}}\|^2}{n} \tag{18}$$

Here, $\boldsymbol{y_m}$ is the true value, $\hat{\boldsymbol{y_m}}$ is the predicted value, and n is the number of training examples. $\|\|$ denotes the L2 norm that measures the distance between two vectors. At the start of training, the weights and biases are randomly initialized and an initial prediction is made using the model. The error function is then computed and the back-propagation
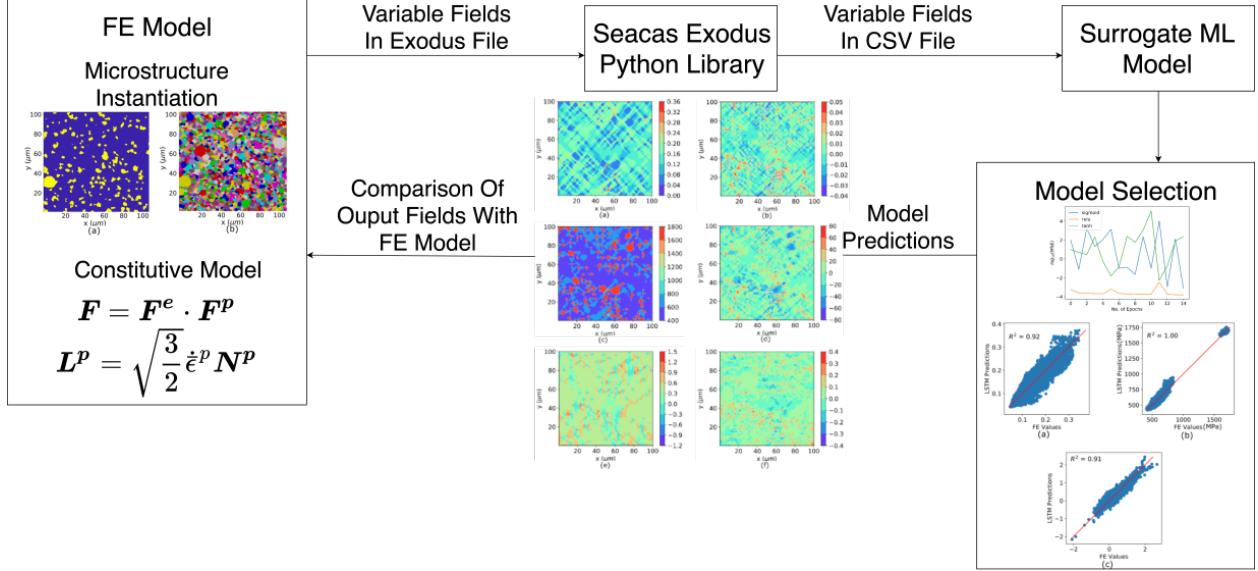
Figure 3: Schematic of integration of the FE framework with the ML-based surrogate modeling framework via the SEACAS library.

algorithm is used to iteratively adjust the weights and biases in each layer, i.e.,

$$\boldsymbol{w} \to \boldsymbol{w}' = \boldsymbol{w} - \eta \boldsymbol{\nabla} C \qquad (19)$$

Here, the learning rate, η, controls the degree by which we want to change our weights after every iteration. Since the magnitudes of the input features (strains and stresses) are expected to be orders of magnitude apart, all the data have been normalized within the range $[0,1]$ in the present work. The normalized value, x_i^n, for any training variable, x_i, is calculated as:

$$x_i^n = \frac{x_i - x_{min}}{x_{max} - x_{min}} \qquad (20)$$

The proposed LSTM model is schematically shown in Figure 4. The output features of interest in the present problem are: effective strain, $\bar{\epsilon}$, von Mises effective stress, $\bar{\sigma}$, and Stress Triaxiality ratio (ST), given as the ratio of the mean stress over the von Mises effective stress. While, effective strain and effective stress can be correlated with plastic deformation in the respective phases, ST provides a measure of the development of multi-axial stresses that may contribute to eventual failure initiation. In the present context, the interfaces between the hard martensite and the soft ferrite phases, where strain partitioning may occur, are potential sites for failure initiation. Hence, it is pertinent to be able to predict the ST.

For each element (material point), the $\bar{\epsilon}$, $\bar{\sigma}$ and ST are exported at nominal strain intervals of 0.01 from the FE results using the SEACAS package. The simulation is run up to 0.15 nominal strain, thus providing us a total of 15 data sets at 0.01 nominal strain intervals. The mesh consists of 400×400 elements, making the length of every feature and output variable as $2,400,000$.

3.2 Surrogate Model Implementation

The LSTM model has been implemented using Google's Tensorflow library [57] with a Keras backend in Python [58]. LSTMs have generally shown great accuracy in predicting sequence and time series data [59, 60]. The evolution of deformation has also been formulated as a sequence modeling problem. As mentioned earlier, we focus on predicting three output variables in our model, namely, effective strain, $\bar{\epsilon}$, von Mises effective stress, $\bar{\sigma}$, and Stress Triaxiality ratio, ST. For a given strain step, t, the input vector, $\boldsymbol{X_t}$, of size $160,000 \times 3$ is input to the LSTM model and used to predict the output vector, $\boldsymbol{Y_t}$, which consists of values at the next strain step in the series X_{t+1}. All data were normalized within the range of $[0,1]$ using equation (20). FE data from the first two strain steps (at 0 and 0.01 nominal strains) were used as input for all LSTM models. The LSTM model is then used to predict the deformation over the remaining strain steps (up to 0.15 nominal strain). The LSTM model, in its present implementation, is thus not a standalone surrogate model and it requires input data from the FE model for the initial strain steps. Possible ways to circumvent this are
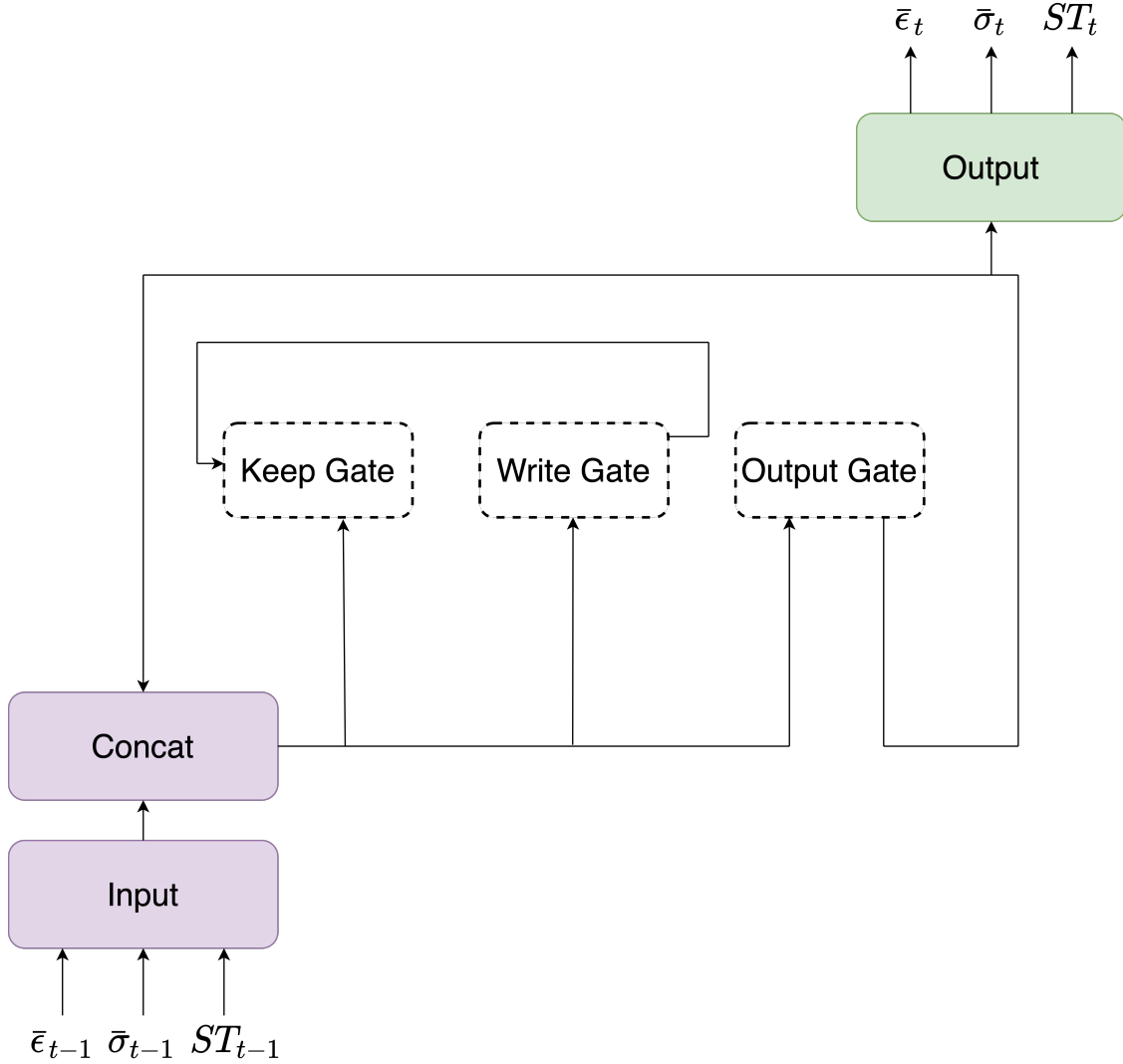
Figure 4: Schematic of the proposed LSTM model.

discussed later. Finally, the microstructure data was split into 70% training, 20% testing, and 10% validation data sets for all models.

4 Results and Discussion

Multiple microstructures have been instantiated using the algorithm described in Section 2.1. Specifically, the grain size ($d_{\alpha\prime}$) and volume fraction (V_α, $V_{\alpha\prime}$) of the constituent phases (ferrite, α, and martensite, $\alpha\prime$) have been varied parametrically. Further, 5 random microstructure instantiations are created for each set of microstructure variables. These set of microstructure variables are listed in table 1 and have been assigned distinct microstructure numbers for future reference. FE simulation results for these 25 microstructures serve as the ground truth for assessing the predictive capabilities of the LSTM models.

Different measures have been used to assess the error associated with the LSTM model predictions, as compared to the ground truth (FE results). They are briefly described in the following.

8

Table 1: Microstructural attributes of the different microstructures considered in the present work in terms of the grain sizes, d, and volume fractions, V, of the constituent phases, α and $\alpha\prime$.

Microstructure #	$d_{\alpha\prime}(\mu m)$	$V_{\alpha\prime}$	$d_{\alpha}(\mu m)$	V_{α}
1,2,3,4,5	1.5	0.13	2.5	0.87
6,7,8,9,10	0.5	0.13	2.5	0.87
11,12,13,14,15	2.5	0.13	2.5	0.87
16,17,18,19,20	1.5	0.2	2.5	0.8
21,22,23,24,25	1.5	0.3	2.5	0.7

The coefficient of determination, R^2, represents the proportion of variance that has been explained by the independent variables in the model and is given by the following equation:

$$R^2(y, \hat{y}) = 1 - \frac{\sum_{m=1}^{n}(y_m - \hat{y}_m)^2}{\sum_{m=1}^{n}(y_m - \bar{y})^2} \tag{21}$$

where, y_m is the actual output (ground true value), and $\hat{y}_m$ is the model prediction. For a model with 100% accuracy, $R^2 = 1$. We also use the Mean Absolute Error (MAE) as an error metric, which is given by the equation:

$$MAE = \frac{\sum_{m=1}^{n}|y_m - \hat{y}_m|}{n} \tag{22}$$

We use R^2 and MAE to assess the performance of the LSTM models for predicting the three output variables: effective strain, $\bar{\epsilon}$, effective stress, $\bar{\sigma}$, and Stress Triaxiality ratio (ST).

4.1 Model Selection

We present LSTM model results for all the microstructures with the different microstructural attributes listed in table 1. Three models with the same architecture, but different training data sets, were trained and their predictions studied. The input to the LSTM model was the effective strain, effective stress and stress triaxiality data obtained from the FE model at the 1st two steps (nominal strain 0 and 0.01) and the LSTM model predicted the corresponding variables at subsequent strain steps. We first present results of the LSTM prediction at the final strain step and then present the model's performance over intermediate strain steps.

While we have tried different model architectures (results not presented here), LSTM model with 8 layers and 100 neurons per layer was found to give predictions with reasonable accuracy. Hence, the same architecture has been used in all our predictions.

Model I was trained only to microstructure #1 and the R^2 and Mean Absolute Error (MAE) values associated with the predictions of the three variables at the final strain step (nominal strain 0.15) are presented in table 2. It can be seen that the R^2 values are generally low for most microstructures, with only a few values above 0.90; R^2 values closer to 1 are desirable. The predictions for microstructures 1 through 5 are somewhat better than the other microstructures because their microstructural attributes are similar to the microstructure used for training. This also suggests that the heterogeneous deformation traits are microstructure-dependent, in addition to being dependent on the mechanical properties of the constituent phases. The relatively higher accuracy observed in the prediction of von Mises effective stress, $\bar{\sigma}$, may be attributed to a lower spread in stress values. The stresses are generally low in the soft ferrite phase and high in the hard martensite phase, with a rather bi-modal distribution. Hence, it easier for the model to predict the effective stress with better accuracy. This will be discussed further in terms of the R^2 plots and deformation contours in the subsequent sections. The data presented in table 2 clearly indicates prediction accuracy for the rest of the microstructures (# 6 through 25) is not good, suggesting the inability of the model to generalize over other data sets.

Model II was trained to microstructure # 1 and # 21 and the corresponding R^2 and Mean Absolute Error (MAE) values associated with the predictions of the three variables at the final strain step are presented in table 3. As can be seen, the prediction accuracy for microstructure # 21 through 25 has now improved, compared to Model I, due to the inclusion of microstructure # 21 in the training data set. The model is now able to predict the change in mechanical properties due to an increase in volume fraction of the hard phase. Physically, an increase in the volume fraction of the hard phase leads to higher overall stresses in the microstructure, and more strain partitioning in the soft phase. The effect of microstructural changes on the deformation characteristics have been described in detail in [46]. However, we observe model II still shows poor accuracy in predicting the deformation in the remaining microstructures. These results clearly indicate that by training the LSTM model to more microstructures with varying attributes, the prediction accuracy for all 25 microstructures may be increased.

Table 2: R^2 and MAE for predictions at the last strain step for the 25 microstructures using LSTM model I, which was trained to microstructure # 1.

Microstructure	$\bar{\epsilon}$		$\bar{\sigma}$		ST	
	R^2	MAE	R^2	MAE (MPa)	R^2	MAE
1	0.88	0.012	0.99	31.303	0.90	0.072
2	0.85	0.012	0.98	34.025	0.92	0.052
3	0.72	0.017	0.90	51.129	0.81	0.0817
4	0.74	0.016	0.84	69.031	0.75	0.113
5	0.81	0.013	0.97	58.959	0.86	0.069
6	0.59	0.0214	0.91	62.380	0.76	0.100
7	0.81	0.0143	0.99	34.737	0.86	0.078
8	0.67	0.019	0.68	85.889	0.60	0.148
9	0.75	0.017	0.96	62.142	0.90	0.061
10	0.60	0.019	0.97	44.194	0.87	0.065
11	0.42	0.025	0.35	124.060	0.67	0.118
12	0.63	0.020	0.60	90.435	0.73	0.111
13	0.83	0.014	0.99	29.540	0.89	0.067
14	0.28	0.024	0.22	132.300	0.07	0.221
15	0.71	0.018	0.98	36.64	0.85	0.077
16	0.80	0.020	0.97	29.932	0.88	0.085
17	0.32	0.031	0.30	155.257	0.82	0.108
18	0.68	0.022	0.73	86.229	0.79	0.120
19	0.70	0.023	0.77	71.911	0.85	0.096
20	0.77	0.019	0.89	45.494	0.87	0.084
21	0.73	0.025	0.67	106.94	0.75	0.14
22	0.85	0.019	0..83	76.413	0.76	0.137
23	0.54	0.033	0.38	169.54	0.75	0.153
24	0.85	0.020	0.84	68.899	0.81	0.126
25	0.77	0.023	0.76	90.865	0.78	0.133

Based on these observations, Model III was trained to data from 5 microstructures, i.e., # 1, # 6, # 11, # 16 and # 21, to account for all the different microstructural attributes studied in the present work and their effect on the ensuing deformation behavior. Essentially, one microstructure from each of the microstructure cases described in table 1 has been used in the training data set. The corresponding R^2 and MAE are presented for the different microstructures in table 4. It can be seen that there is a clear increase in the prediction accuracy for all microstructures using model III. The R^2 increases and the MAE decreases as compared to model I and II. Apart from microstructure # 10 and 17, the R^2 in prediction of $\bar{\epsilon}$ is greater than 0.8, while that for $\bar{\sigma}$ is greater than 0.95, and for ST is greater than 0.84. While the purpose of this manuscript is only to give a proof-of-concept demonstration of the LSTM model, the prediction accuracy may be further increased by training the LSTM model to more microstructures, perhaps two instantiations per microstructure attribute, thus allowing the ML model to further generalize the structure-property correlations in these dual phase microstructures. The only trade off with increasing the training data is the increase in training time. However, once trained, the same LSTM model can be used for multiple microstructure predictions, without affecting the prediction time. These are discussed in more detail later.

Further, we graphically present R^2 values for two microstructures to which the model III has not been trained. We choose microstructure # 14 and # 17 for this purpose. As seen in table 4, microstructure # 14 shows relatively lower error in prediction as compared to the other untrained microstructures, while microstructure # 17 shows the relatively higher errors. Figure 5 shows the LSTM predicted values versus FE values for all three output variables at the last strain step for microstructure # 14, and figure 6 shows the same for microstructure # 17. It can be seen that the spread in values of the $y = x$ line is relatively lower for the effective strain in 5(a) as compared to 6(a). The LSTM model under-predicts the effective strain for microstructure #17. However, there appears to be qualitative concurrence between the LSTM predicted values and the FE values over the entire range of effective strain in both cases, even though the R^2 values are somewhat low for one case. Similar observations can be made in the prediction of stress triaxiality ratios as well. The LSTM predicted values for effective stress appear to be in quantitative concurrence with the FE values in both cases. As mentioned earlier, there is stress partitioning between the hard and soft phases and there are no intermediate values for stress. Given this bi-modal distribution and a relatively low scatter in the data, the LSTM model is able to train and predict the effective stress values with reasonable accuracy.
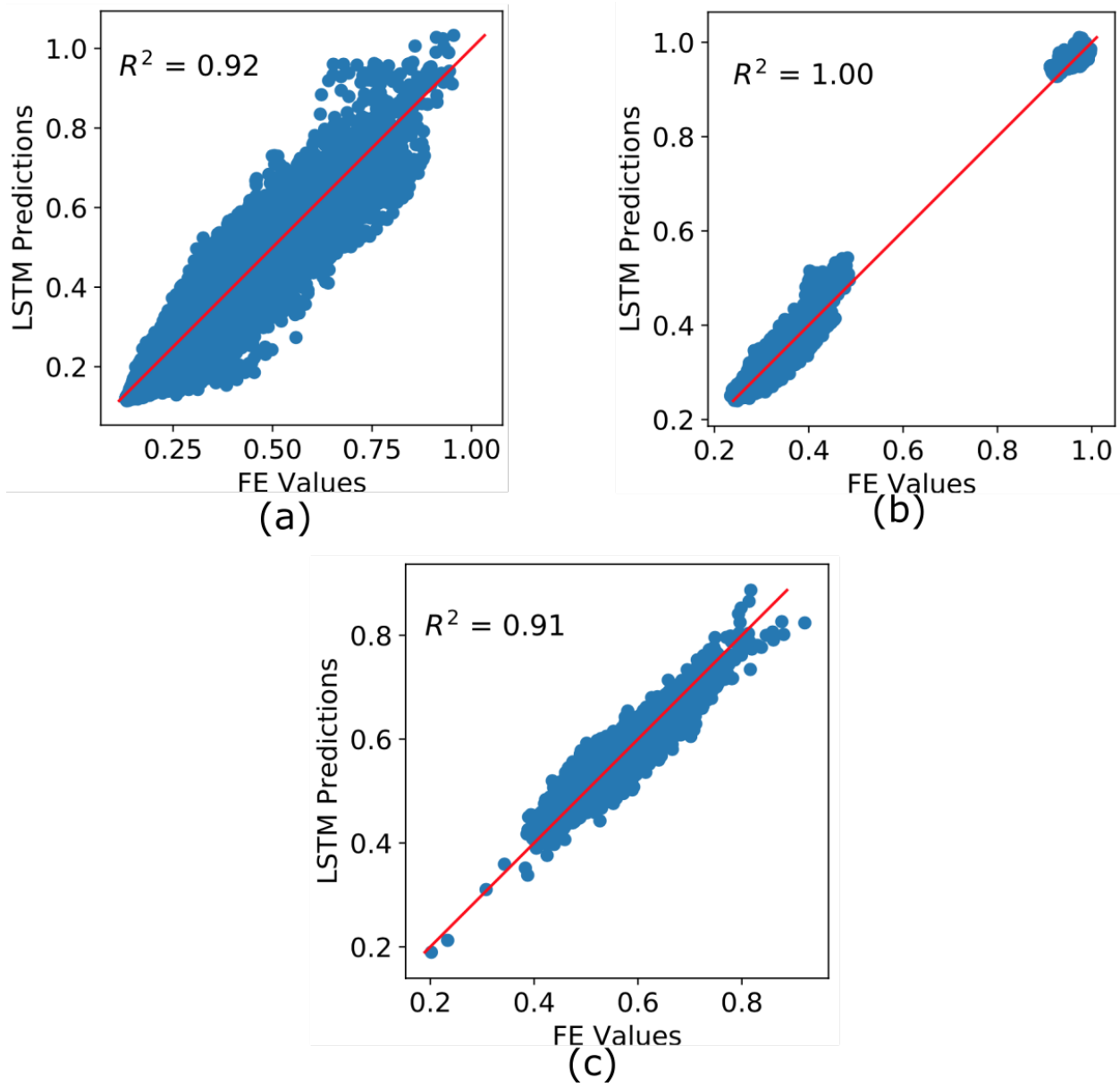
Figure 5: Plot of LSTM predicted values vs FE values for (a) effective strain, (b) von Mises effective stress, (c) triaxiality for microstructure # 14.
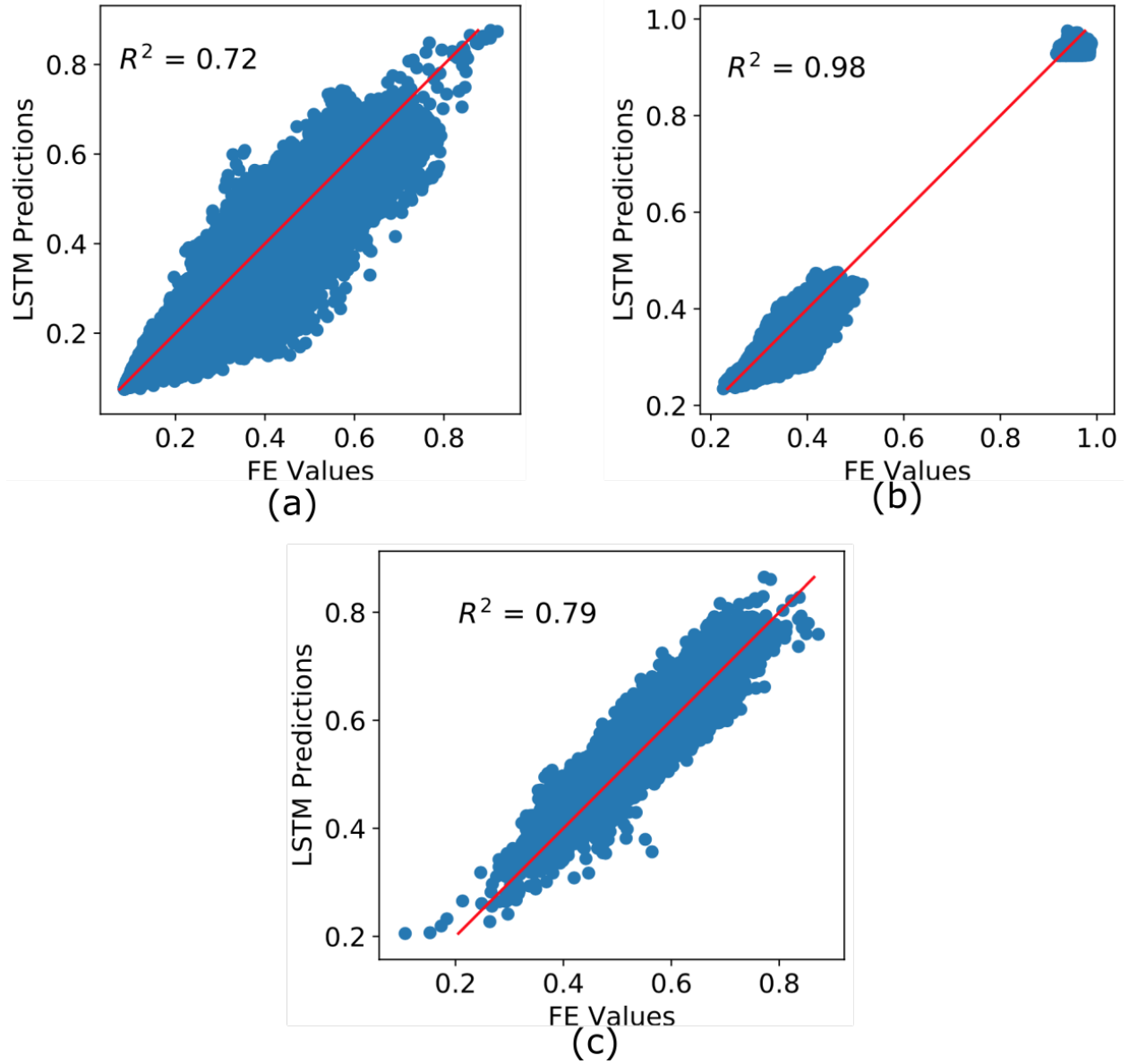
Figure 6: Plot of LSTM predicted values vs FE values for (a) effective strain, (b) von Mises effective stress, (c) triaxiality for microstructure # 17.

Table 3: R^2 and MAE for predictions at the last strain step for the 25 microstructures using LSTM model II, which was trained to microstructure # 1 and # 21.

| Microstructure | $\bar{\epsilon}$ | | $\bar{\sigma}$ | | ST | |
	R^2	MAE	R^2	MAE (MPa)	R^2	MAE
1	0.92	0.010	0.99	14.923	0.93	0.053
2	0.83	0.013	0.96	61.048	0.90	0.058
3	0.60	0.021	0.98	39.241	0.52	0.147
4	0.71	0.0176	0.96	60.185	0.42	0.179
5	0.83	0.014	0.94	77.031	0.86	0.073
6	0.52	0.025	0.86	123.281	0.64	0.11
7	0.77	0.017	0.92	96.019	0.80	0.904
8	0.71	0.020	0.91	99.270	0.53	0.144
9	0.78	0.017	0.95	74.293	0.87	0.067
10	0.65	0.019	0.91	93.678	0.83	0.073
11	0.59	0.030	0.85	100.121	0.39	0.120
12	0.67	0.020	0.92	89.124	0.46	0.156
13	0.77	0.017	0.93	88.653	0.80	0.091
14	0.28	0.021	0.49	65.094	-1.00	0.272
15	0.62	0.023	0.90	107.619	0.72	0.107
16	0.69	0.027	0.99	35.869	0.89	0.085
17	0.77	0.020	0.98	50.113	0.78	0.112
18	0.80	0.020	0.95	89.889	0.71	0.128
19	0.75	0.023	0.97	75.312	0.78	0.112
20	0.78	0.020	0.96	69.291	0.85	0.091
21	0.88	0.017	0.99	24.95	0.89	0.090
22	0.85	0.019	0.98	39.73	0.80	0.123
23	0.86	0.019	0.99	31.062	0.87	0.098
24	0.80	0.024	0.98	45.25	0.80	0.142
25	0.87	0.017	0.99	26.22	0.90	0.090

4.2 Error in Prediction at Intermediate Steps

We now present results for the LSTM model III predictions at the intermediate steps. Figure 7 shows a box plot of the mean absolute error (MAE) values for the three output variables: (a) $\bar{\epsilon}$, (b) $\bar{\sigma}$, and (c) ST at every time step for all the 25 microstructures. This is plotted using the MAEs for all material points and all 15 time steps for each of the three output variables. Essentially, this comprises data from $160,000 \times 15$ elements for each output variable for each microstructure.

It can be seen that the MAE in prediction is relatively low for the training microstructures (microstructure # 1, 6, 11, 16, 21) for all three variables. For example, the MAE in effective stress prediction is lower than 20 MPa, whereas the actual values of stress may reach 1800 MPa (cf. figure 2). The error in prediction of stress is lower than 80 MPa even for the untrained microstructures. The MAE in the prediction of effective strain is lower than 0.02 for most cases, andfor the prediction of stress triaxiality ratio is lower than 0.12. Again the actual effective strain values may go as high as 0.45, while the stress triaxiality ratio may lie in the range -1.5 to 2.5 (cf. figure 2). Hence, the MAE in predictions is lower than $\approx 10\%$ for all variables for all microstructures.

Based on these results, we conclude that the ability of the LSTM model III to accurately predict the structure-property correlations increases due to the consideration of additional cases with different microstructural attributes in the training data set. It is worth noting that while capturing history dependence is an inherent trait of LSTM models, the model's ability to account for the effect of spatial heterogeneity on structure-property correlations appears remarkable as well. The LSTM model is able to accomplish this simply by training to the data sequences across different microstructures with varying deformation traits.

4.3 LSTM Prediction of Deformation Contours

In order to demonstrate the model's predictive capabilities, we present the deformation contours for a microstructure to which the model III has not been trained. We choose microstructure # 14 for this purpose. Note that model III has only
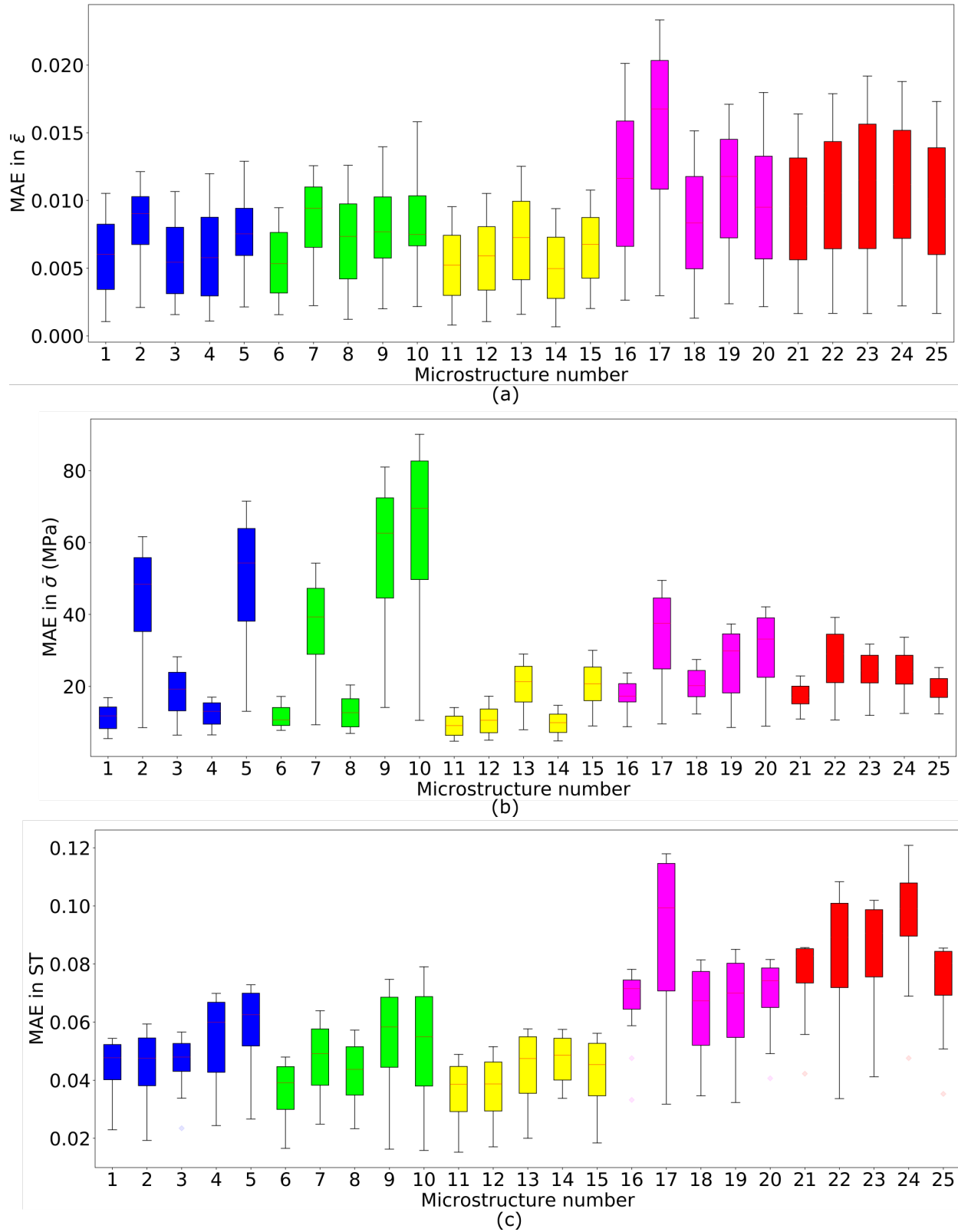
Figure 7: Box plots of mean average error (MAE) for LSTM model III predicted values for (a) $\bar{\epsilon}$, (b) $\bar{\sigma}$, and (c) ST across all material points and all strain steps for the different microstructures. The different colors in the box plots are used to denote the different microstructure attributes considered in table 1.

14

Table 4: R^2 and MAE for predictions at the last strain step for the 25 microstructures using LSTM model III, which was trained to microstructure # 1, # 6, # 11, # 16 and # 21.

Microstructure	$\bar{\epsilon}$		$\bar{\sigma}$		ST	
	R^2	MAE	R^2	MAE (MPa)	R^2	MAE
1	0.91	0.010	0.99	16.874	0.93	0.054
2	0.86	0.012	0.96	61.623	0.89	0.059
3	0.89	0.010	0.99	28.221	0.91	0.056
4	0.87	0.011	0.99	17.001	0.89	0.069
5	0.84	0.012	0.95	71.509	0.85	0.072
6	0.91	0.009	0.99	17.191	0.93	0.048
7	0.87	0.012	0.97	54.258	0.90	0.063
8	0.87	0.012	0.99	20.403	0.92	0.057
9	0.83	0.013	0.95	80.992	0.84	0.074
10	0.74	0.015	0.92	90.096	0.81	0.079
11	0.92	0.009	0.99	14.130	0.93	0.048
12	0.90	0.010	0.99	17.262	0.92	0.051
13	0.86	0.012	0.99	28.989	0.92	0.057
14	0.92	0.009	0.99	14.725	0.91	0.057
15	0.90	0.010	0.99	30.021	0.91	0.056
16	0.81	0.020	0.99	23.751	0.90	0.078
17	0.72	0.023	0.98	49.489	0.78	0.117
18	0.87	0.015	0.99	27.456	0.88	0.081
19	0.86	0.017	0.99	37.360	0.88	0.085
20	0.83	0.018	0.99	42.115	0.88	0.081
21	0.90	0.016	0.99	22.904	0.90	0.085
22	0.88	0.017	0.99	39.181	0.85	0.108
23	0.86	0.019	0.99	31.765	0.87	0.101
24	0.87	0.018	0.99	33.653	0.85	0.120
25	0.89	0.017	0.99	25.252	0.91	0.085

been trained to microstructure # 1, 6, 11, 16 and 21. Hence, the local mechanical properties for microstructure # 14 are expected to be distinct from any of the training microstructures.

Contour plots of LSTM predictions and the associated errors at the last strain step are shown in figure 8 for: (a) $\bar{\epsilon}$, (c) $\bar{\sigma}$, and (e) ST, respectively. The corresponding errors in prediction are shown in figure 8 (b), (d), and (f) for $\bar{\epsilon}$, $\bar{\sigma}$, and ST, respectively. It is clear from figure 8(a) and (b) that the LSTM model is able to predict the strain localization trends with reasonable accuracy. For example, while the maximum value of $\bar{\epsilon}$ is 0.36, the range of associated error is $[-0.040, 0.05]$. Similarly, figure 8(d) shows that the error in prediction of $\bar{\sigma}$ is negligible. While the maximum $\bar{\sigma}$ is of the order of 1800 MPa, the scale for error contours lies in the range $[-80, 80]$ MPa. The ST contour and the associated error also demonstrates similar trends. It should also be noted that the deformation contours for this microstructure (# 14, $d_{\alpha'}$ of 2.5 (μm)) are quite distinct from that presented in figure 2 for microstructure # 1, with $d_{\alpha'}$ of 1.5 (μm). The FE model accounts for grain size-dependent Hall-Petch hardening (cf. [46]) and hence gives lower stresses in the hard phase for microstructure # 14. Although the strain localizations and stress hot spots appear very distinct in these two microstructures, the LSTM model gives accurate predictions of the deformation contours in the untrained microstructure. Generally speaking, the LSTM model III is able to predict the heterogeneous deformation contours in an untrained microstructure with high accuracy.

We have also used the LSTM model III to predict the strain contours at intermediate strain steps. The LSTM predicted contours of $\bar{\epsilon}$ are shown in figure 9(a) and 9(c) for 0.05 and 0.10 nominal strain, respectively, along with the associated errors in figure 9(c) and 9(d), respectively. It can be seen from the error contours at both these nominal strains that the associated errors are relatively low. These results indicate the LSTM model's capability to predict the spatio-temporal evolution of heterogeneous deformation fields in dual phase microstructures with high accuracy.

4.4 LSTM Prediction of Aggregate Properties

Finally, we have used the LSTM predicted contours to calculate the average values of $\bar{\sigma}$ and $\bar{\epsilon}$ at each strain step. These are then used to re-construct the ensemble-average stress-strain response. Figure 10(a) shows a comparison of
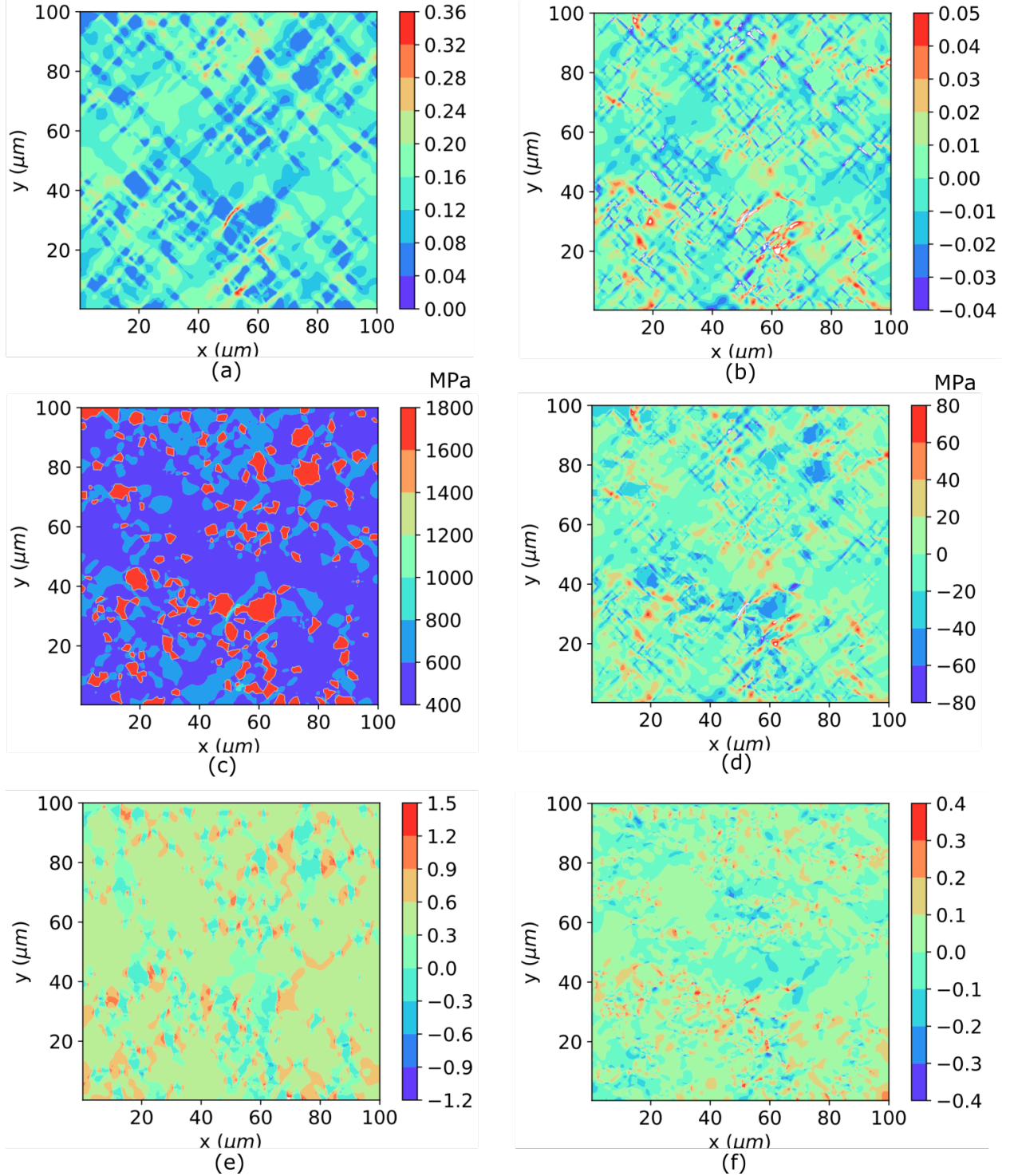
Figure 8: Spatial contours of LSTM model III predicted values for (a) $\bar{\epsilon}$, (c) $\bar{\sigma}$, and (e) ST for microstructure # 14. The corresponding error contours are plotted in (b) $\bar{\epsilon}$, (d) $\bar{\sigma}$, and (f) ST. Note that model III has not been trained to this microstructure.
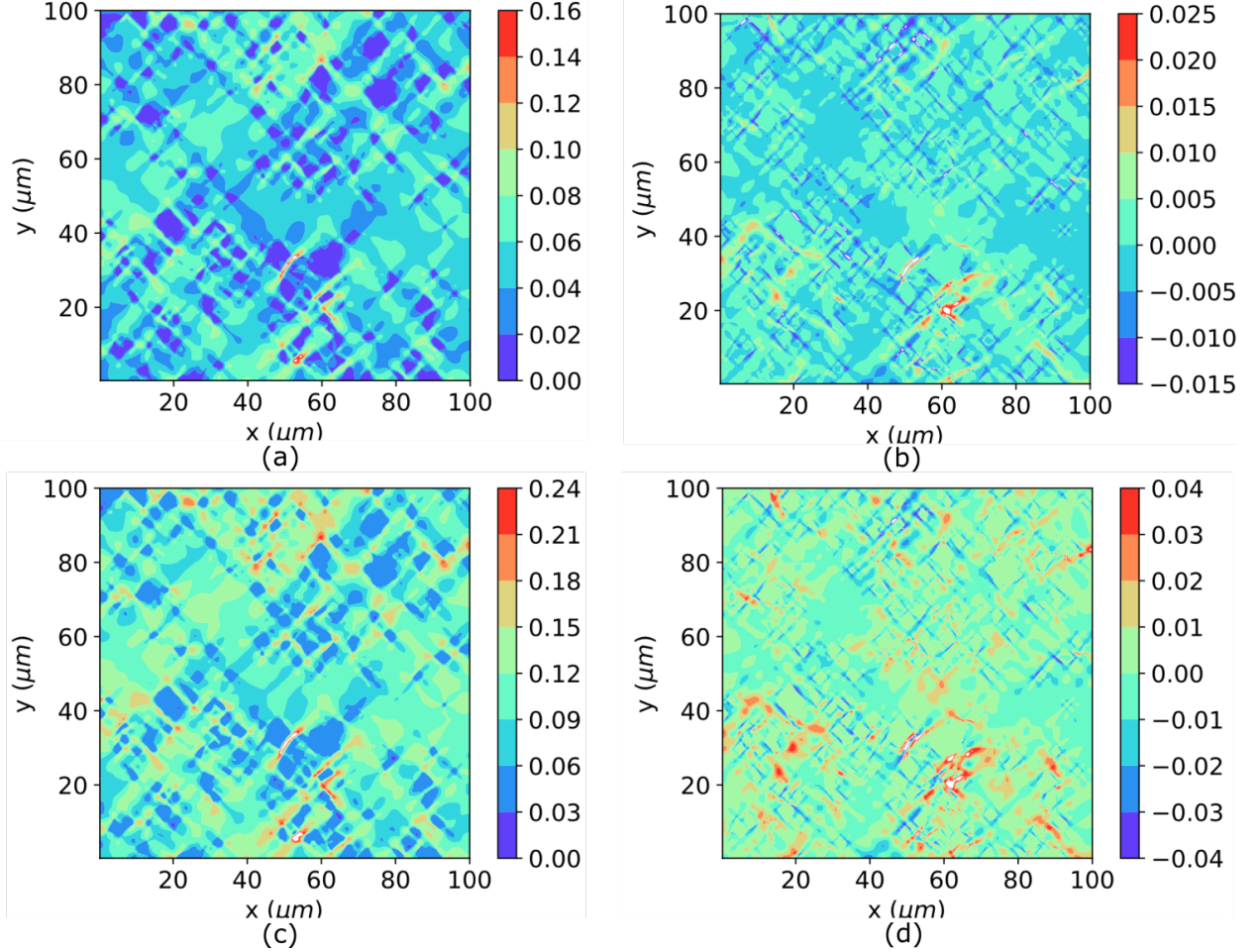
Figure 9: Spatial contours of LSTM model III predicted values for $\bar{\epsilon}$ at (a) 0.05 nominal strain, and (c) 0.10 nominal strain for the untrained microstructure # 14. The corresponding error contours are plotted in (b) and (d), respectively.

the LSTM predicted stress-strain response with the 'ground truth' FE stress-strain response. It can be seen that the LSTM-predicted aggregate response compares very well with the FE response.

Strain partitioning is a commonly observed phenomenon in these dual phase microstructures [17]. This occurs due to higher deformation being accommodated in the softer phase. On the other hand, the harder phase, with a relatively higher yield stress, does not accommodate much deformation and primarily contributes to strengthening of the microstructure. Figure 10(b) shows the comparison of the LSTM predicted and FE predicted average effective strains in the soft and the hard phases as a function of nominal strain. It can be seen that the LSTM model is marginally under-predicting the average strain in the both the phases as compared to the FE values, while qualitatively predicting the expected trends. The strain partitioning effect due to the presence of a hard and soft phase in the dual phase microstructure is clearly visible from these plots. Underlying mechanisms are discussed in more detail in the next section.

Overall, we have demonstrated the LSTM model's capabilities of predicting the local and aggregate mechanical properties of dual phase microstructures with varying attributes, such as constituent grain sizes and constituent volume fractions.

4.5 Discussion

The application problem chosen in this work is the elastic-plastic deformation of a two phase microstructure. This microstructure is representative of Dual Phase (DP) steels, comprised of the soft ferrite phase and the relatively harder martensite phase. Since there is a large strength differential between the phases (> 1 GPa), the stress is usually
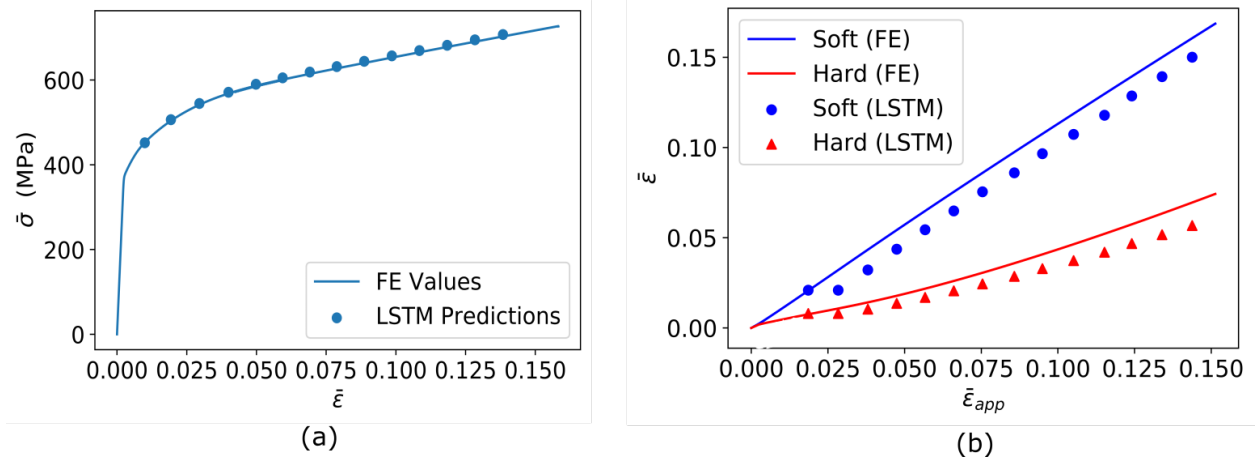
Figure 10: (a) Comparison of re-constructed stress-strain curve from LSTM model III predictions with the FE results for the untrained microstructure # 14. (b) Average effective strains in the soft ferrite and hard martensite phases as a function of nominal strain as predicted using the LSTM model III and the FE model for the same microstructure.

partitioned to the hard martensite phase, while the strain is partitioned to the softer ferrite phase. This was also observed in our simulations (cf. figure 10(b)). At the early stages of deformation, the ferrite phase starts to deform plastically due to its lower yield strength, while the martensite still deforms elastically. At the later stages, the martensite phase also starts to show some plastic deformation, although with limited strain hardening [61, 62] due to its complex hierarchical structure [63, 64]. As the ferrite phase deforms plastically, accumulation of dislocation forests lead to large amounts of strain hardening, especially in the ferrite grains lying between closely spaced martensite islands. Eventually, the strength differential between the two phases is reduced and the strain also starts to partition to the martensite phase [65, 66]. Severe strain localization occurs, especially at the corners of sharp martensite islands, which act as hot spots for eventual nucleation of damage [62, 66].

It is therefore important to predict such hot spots for large microstructures using computationally efficient techniques, such as ML-based surrogate models. Predicting the same for large dual phase microstructures, with heterogeneous deformation characteristics, may perhaps be too computationally expensive for physics-based FE frameworks. As a comparison, each of the FE simulations took ≈ 1440 compute hours (60 physical hours for a simulation running on 24 core Intel Xeon processors and 4 GB memory per core) to reach 0.15 nominal strain. In contrast, the LSTM model III was trained in less than ≈ 28 compute hours (3.5 physical hours for a training running on a workstation computer with 8 core Intel i7 processor and 2 GB memory per core). Once trained, the LSTM model III was able to predict the deformation contours in less than 5 minutes on the workstation computer. This amounts to a speed up of ≈ 50 times as compared to the FE simulations, including the training time (which only needs to be performed once per model). Excluding training time, the speed up is greater than ≈ 2000 times.

However, one drawback with the present implementation of the LSTM model is that it still needs data from the FE simulations for the first two strain steps as an input. Hence, it not possible to completely bypass the FE simulations at the moment. In order to develop a standalone surrogate model, a hybrid ML model using a combination of ANN (for establishing correlations between the microstructural attributes and mechanical properties) and LSTM for predicting history-dependent deformation maybe developed. Other variants of LSTM, such as Fully Connected LSTM (FC-LSTM) or Convolutional LSTM (ConvLSTM) [55] may also be explored for this purpose in the future. A larger data set, comprising of multiple microstructures, may also help in reducing the errors associated with over-fitting, if any.

The LSTM model III predicts all three output variables with reasonable accuracy for trained as well untrained microstructures. Plastic deformation being a history-dependent process, this behavior is better modeled using LSTM networks, as they treat the data as a time series. LSTMs maintain a context over time, thus making them efficient in time series predictive modeling problems. Pandey and Pokharel [27] used a similar approach to predict the evolution of crystallographic orientation in polycrystalline ensembles undergoing plastic deformation. Their model also considers data from the nearest neighbourhood to predict the orientation evolution at any material point. In comparison, our LSTM model is much simpler and does not consider the effect of neighbors. Logarzo et al. [33] also used sequence to sequence modeling to develop Smart Constitutive Laws (SCLs) to predict the response of any material given the loading histories. They generate a number strain sequences which are used as inputs to predict the stress response.

18

Their model establishes a relationship between the strain sequences and the corresponding stresses, thus acting as an 'effective' constitutive law. In contrast, our approach predicts all variables independently only using their individual histories as inputs.

5   Conclusions

We have developed a Machine Learning (ML)-based surrogate modeling framework to predict the deformation of dual phase microstructures. Long Short Term Memory (LSTM) based ML models, trained with different data sets, have been used to predict three output variables: effective strain, $\bar{\epsilon}$, effective stress, $\bar{\sigma}$, and Stress Triaxiality ratio, ST, and their prediction efficacy compared with the ground truth results. The results from a microstructure-sensitive, J2 plasticity-based Finite Element (FE) simulations are used as the ground truth for the LSTM model training and prediction.

- Model I, which was trained to only 1 microstructure, was unable to make predictions for the untrained microstructures. Presumably, the model was over-fit to the training microstructure, with no ability to generalize over other microstructures.

- As the LSTM model was trained to more number of microstructures in model II and III, it's ability to generalize the structure-property correlations in untrained microstructures improved significantly.

- Model III was trained to 5 different microstructures, in order to improve it's predictive capabilities for untrained microstructures. The model successfully predicted all three output variables for 25 distinct microstructures, with different grain sizes, volume fractions and random instantiations, at every strain step with reasonable accuracy.

- Model III was also able to predict the ensemble average properties, such as the stress-strain response and strain partitioning for an untrained microstructure, with reasonable accuracy.

- The LSTM model gives a significant speed up over the FE model for prediction of deformation in dual phase microstructures.

The application of LSTM-based ML models for predicting the spatio-temporal contours of dual phase microstructures during elastic-plastic deformation is the novelty of our work. While Pandey and Pokharel [27] demonstrated the same for single phase microstructures, we have demonstrated the applicability of LSTM networks for dual phase microstructures and predicted three output variables simultaneously for several untrained microstructures.

6   Acknowledgements

7   Declaration of Competing Interest

The authors declare that they have no known competing financial interests or personal relationships that could have appeared to influence the work reported in this paper.

8   Data Availability

The data presented in this work will be made available on reasonable request.

References

[1] Marko Knezevic, Justin Crapps, Irene J. Beyerlein, Daniel R. Coughlin, Kester D. Clarke, and Rodney J. McCabe. Anisotropic modeling of structural components using embedded crystal plasticity constructive laws within finite elements. *International Journal of Mechanical Sciences*, 105:227 – 238, 2016.

[2] Anirban Patra and Carlos N Tomé. Finite element simulation of gap opening between cladding tube and spacer grid in a fuel rod assembly using crystallographic models of irradiation growth and creep. *Nuclear Engineering and Design*, 315:155–169, 2017.

[3] Franz Roters, Philip Eisenlohr, Luc Hantcherli, Denny Dharmawan Tjahjanto, Thomas R Bieler, and Dierk Raabe. Overview of constitutive laws, kinematics, homogenization and multiscale methods in crystal plasticity finite-element modeling: Theory, experiments, applications. *Acta Materialia*, 58(4):1152–1211, 2010.

[4] Khushahal Thool, Anirban Patra, David Fullwood, K.V. Mani Krishna, Dinesh Srivastava, and Indradev Samajdar. The role of crystallographic orientations on heterogeneous deformation in a zirconium alloy: A combined experimental and modeling study. *International Journal of Plasticity*, 133:102785, 2020.

[5] CR Mayer, LW Yang, SS Singh, J Llorca, JM Molina-Aldareguia, YL Shen, and Nikhilesh Chawla. Anisotropy, size, and aspect ratio effects on micropillar compression of alsic nanolaminate composites. *Acta Materialia*, 114:25–32, 2016.

[6] JA Knapp, DM Follstaedt, SM Myers, JC Barbour, and TA Friedmann. Finite-element modeling of nanoindentation. *Journal of Applied Physics*, 85(3):1460–1474, 1999.

[7] Nader Zaafarani, Dierk Raabe, Ripandeep N Singh, F Roters, and S Zaefferer. Three-dimensional investigation of the texture and microstructure below a nanoindent in a cu single crystal using 3d ebsd and crystal plasticity finite element simulations. *Acta Materialia*, 54(7):1863–1876, 2006.

[8] David L McDowell. Viscoplasticity of heterogeneous metallic materials. *Materials Science and Engineering: R: Reports*, 62(3):67–123, 2008.

[9] Omid Sedaghat and Hamidreza Abdolvand. A non-local crystal plasticity constitutive model for hexagonal close-packed polycrystals. *International Journal of Plasticity*, 136:102883, 2021.

[10] Michael R Tonks, Derek Gaston, Paul C Millett, David Andrs, and Paul Talbot. An object-oriented finite element framework for multiphysics phase field simulations. *Computational Materials Science*, 51(1):20–29, 2012.

[11] Sanghyun Lee, Mary F Wheeler, and Thomas Wick. Pressure and fluid-driven fracture propagation in porous media using an adaptive finite element phase field model. *Computer Methods in Applied Mechanics and Engineering*, 305:111–132, 2016.

[12] SeonHong Na and WaiChing Sun. Computational thermomechanics of crystalline rock, part i: A combined multi-phase-field/crystal plasticity approach for single crystal simulations. *Computer Methods in Applied Mechanics and Engineering*, 338:657–691, 2018.

[13] Chuanlai Liu, Pratheek Shanthraj, Martin Diehl, Franz Roters, S Dong, Jie Dong, Wenjiang Ding, and Dierk Raabe. An integrated crystal plasticity–phase field model for spatially resolved twin nucleation, propagation, and growth in hexagonal materials. *International Journal of Plasticity*, 106:203–227, 2018.

[14] Ricardo A. Lebensohn, Anand K. Kanjarla, and Philip Eisenlohr. An elasto-viscoplastic formulation based on fast fourier transforms for the prediction of micromechanical fields in polycrystalline materials. *International Journal of Plasticity*, 32-33:59 – 69, 2012.

[15] Ricardo A Lebensohn and Alan Needleman. Numerical implementation of non-local polycrystal plasticity using fast fourier transforms. *Journal of the Mechanics and Physics of Solids*, 97:333–351, 2016.

[16] Aldo Marano, Lionel Gélébart, and Samuel Forest. Fft-based simulations of slip and kink bands formation in 3d polycrystals: influence of strain gradient crystal plasticity. *Journal of the Mechanics and Physics of Solids*, page 104295, 2021.

[17] Cemal Cem Tasan, Martin Diehl, Dingshun Yan, Claudio Zambaldi, Pratheek Shanthraj, Franz Roters, and Dierk Raabe. Integrated experimental–simulation analysis of stress and strain partitioning in multiphase alloys. *Acta Materialia*, 81:386–400, 2014.

[18] Reeju Pokharel, Anirban Patra, Donald W. Brown, Bjørn Clausen, Sven C. Vogel, and George T. Gray. An analysis of phase stresses in additively manufactured 304l stainless steel using neutron diffraction measurements and crystal plasticity finite element simulations. *International Journal of Plasticity*, 121:201 – 217, 2019.

[19] Emily Ford, Kailasnath Maneparambil, Subramaniam Rajan, and Narayanan Neithalath. Machine learning-based accelerated property prediction of two-phase materials using microstructural descriptors and finite element analysis. *Computational Materials Science*, 191:110328, 2021.

[20] Sepideh Hashemi and Surya R Kalidindi. A machine learning framework for the temporal evolution of microstructure during static recrystallization of polycrystalline materials simulated by cellular automaton. *Computational Materials Science*, 188:110132, 2021.

[21] Anuradha Beniwal, Ritesh Dadhich, and Alankar Alankar. Deep learning based predictive modeling for structure-property linkages. *Materialia*, 8:100435, 2019.

[22] Ruoqian Liu, Yuksel C Yabansu, Ankit Agrawal, Surya R Kalidindi, and Alok N Choudhary. Machine learning approaches for elastic localization linkages in high-contrast composite materials. *Integrating Materials and Manufacturing Innovation*, 4(1):192–208, 2015.

[23] Ankit Agrawal and Alok Choudhary. Perspective: Materials informatics and big data: Realization of the "fourth paradigm" of science in materials science. *Apl Materials*, 4(5):053208, 2016.

[24] Ruoqian Liu, Yuksel C Yabansu, Zijiang Yang, Alok N Choudhary, Surya R Kalidindi, and Ankit Agrawal. Context aware machine learning approaches for modeling elastic localization in three-dimensional composite microstructures. *Integrating Materials and Manufacturing Innovation*, 6(2):160–171, 2017.

[25] Ankita Mangal and Elizabeth A. Holm. Applied machine learning to predict stress hotspots i: Face centered cubic materials. *International Journal of Plasticity*, 111:122 – 134, 2018.

[26] Xiang Li, Zhanli Liu, Shaoqing Cui, Chengcheng Luo, Chenfeng Li, and Zhuo Zhuang. Predicting the effective mechanical property of heterogeneous materials by image based modeling and deep learning. *Computer Methods in Applied Mechanics and Engineering*, 347:735–753, 2019.

[27] Anup Pandey and Reeju Pokharel. Machine learning enabled surrogate crystal plasticity model for spatially resolved 3d orientation evolution under uniaxial tension. *arXiv preprint arXiv:2005.00951*, 2020.

[28] Anup Pandey and Reeju Pokharel. Machine learning based surrogate modeling approach for mapping crystal deformation in three dimensions. *Scripta Materialia*, 193:1–5, 2021.

[29] Waqas Muhammad, Abhijit P Brahme, Olga Ibragimova, Jidong Kang, and Kaan Inal. A machine learning framework to predict local strain distribution and the evolution of plastic anisotropy & fracture in additively manufactured alloys. *International Journal of Plasticity*, page 102867, 2020.

[30] Akash Gupta, Ahmet Cecen, Sharad Goyal, Amarendra K Singh, and Surya R Kalidindi. Structure–property linkages using a data science approach: application to a non-metallic inclusion/steel composite system. *Acta Materialia*, 91:239–254, 2015.

[31] Trenton Kirchdoerfer and Michael Ortiz. Data-driven computational mechanics. *Computer Methods in Applied Mechanics and Engineering*, 304:81–101, 2016.

[32] Aaron E Tallman, M Arul Kumar, Andrew Castillo, Wei Wen, Laurent Capolungo, and Carlos N Tomé. Data-driven constitutive model for the inelastic response of metals: Application to 316h steel. *Integrating Materials and Manufacturing Innovation*, 9(4):339–357, 2020.

[33] Hernan J Logarzo, German Capuano, and Julian J Rimoli. Smart constitutive laws: Inelastic homogenization through machine learning. *Computer Methods in Applied Mechanics and Engineering*, 373:113482, 2021.

[34] Michael I Jordan and Tom M Mitchell. Machine learning: Trends, perspectives, and prospects. *Science*, 349(6245):255–260, 2015.

[35] Dane Morgan and Ryan Jacobs. Opportunities and challenges for machine learning in materials science. *Annual Review of Materials Research*, 50:71–103, 2020.

[36] Sepp Hochreiter and Jürgen Schmidhuber. Long short-term memory. *Neural computation*, 9(8):1735–1780, 1997.

[37] Xueyang Li, Christian C Roth, and Dirk Mohr. Machine-learning based temperature-and rate-dependent plasticity model: application to analysis of fracture experiments on dp steel. *International Journal of Plasticity*, 118:320–344, 2019.

[38] RB Vieira and J Lambros. Machine learning neural-network predictions for grain-boundary strain accumulation in a polycrystalline metal. *Experimental Mechanics*, 61(4):627–639, 2021.

[39] Frederic E Bock, Roland C Aydin, Christian J Cyron, Norbert Huber, Surya R Kalidindi, and Benjamin Klusemann. A review of the application of machine learning and data mining approaches in continuum materials mechanics. *Frontiers in Materials*, 6:110, 2019.

[40] Esteban Samaniego, Cosmin Anitescu, Somdatta Goswami, Vien Minh Nguyen-Thanh, Hongwei Guo, Khader Hamdia, X Zhuang, and T Rabczuk. An energy approach to the solution of partial differential equations in computational mechanics via machine learning: Concepts, implementation and applications. *Computer Methods in Applied Mechanics and Engineering*, 362:112790, 2020.

[41] Ari L Frankel, Reese E Jones, Coleman Alleman, and Jeremy A Templeton. Predicting the mechanical response of oligocrystals with deep learning. *Computational Materials Science*, 169:109099, 2019.

[42] MV Pathan, SA Ponnusami, J Pathan, R Pitisongsawat, B Erice, N Petrinic, and VL Tagarielli. Predictions of the mechanical properties of unidirectional fibre composites by supervised machine learning. *Scientific reports*, 9(1):1–10, 2019.

[43] Anirban Patra, Matthew W Priddy, and David L McDowell. Modeling the effects of microstructure on the tensile properties and micro-fracture behavior of mo–si–b alloys at elevated temperatures. *Intermetallics*, 64:6–17, 2015.

[44] Csimsoft Trelis. Advanced meshing for challenging simulations (2013-2016).

[45] Brett D Ellis, Hasan Haider, Matthew W Priddy, and Anirban Patra. Integrated computational design of three-phase mo–si–b alloy turbine blade for high-temperature aerospace applications. *Integrating Materials and Manufacturing Innovation*, 10(2):245–264, 2021.

[46] Soudip Basu, Anirban Patra, Balila Nagamani Jaya, Sarbari Ganguly, Monojit Dutta, and Indradev Samajdar. Computational modeling of microstructure-property correlations in dual phase (dp) steels for achieving enhanced strength and reduced strain partitioning. *Manuscript submitted*, 2021.

[47] Devraj Ranjan, Sankar Narayanan, Kai Kadau, and Anirban Patra. Crystal plasticity modeling of non-schmid yield behavior: from ni3al single crystals to ni-based superalloys. *Modelling and Simulation in Materials Science and Engineering*, 29:055005, 2021.

[48] U.F. Kocks, A.S. Argon, and M.F. Ashby. Thermodynamics and kinetics of slip. *Progress in Materials Scince*, 19:1–288, 1975.

[49] Soudip Basu, Anirban Patra, Jaya Balila Nagamani, and Indradev Samajdar. A computational modeling framework for studying the microstructural factors inducing strain partitioning in dual phase steels. *manuscript in preparation*.

[50] Cody J. Permann, Derek R. Gaston, David Andrš, Robert W. Carlsen, Fande Kong, Alexander D. Lindsay, Jason M. Miller, John W. Peterson, Andrew E. Slaughter, Roy H. Stogner, and Richard C. Martineau. MOOSE: Enabling massively parallel multiphysics simulation. *SoftwareX*, 11:100430, 2020.

[51] William C Mills-Curran, Amy P Gilkey, and Dennis P Flanagan. Exodus: A finite element file format for pre-and postprocessing. Technical report, Sandia National Labs., Albuquerque, NM (USA), 1988.

[52] Greg Sjaardema. Sandia engineering analysis code access system (seacas), 2020(accessed June 5, 2020). https://github.com/gsjaardema/seacas.

[53] Nikhil Buduma and Nicholas Locascio. *Fundamentals of deep learning: Designing next-generation machine intelligence algorithms*. " O'Reilly Media, Inc.", 2017.

[54] Alex Graves. *Supervised Sequence Labelling with Recurrent Neural Networks*. Studies in computational intelligence. Springer, Berlin, 2012.

[55] Xingjian Shi, Zhourong Chen, Hao Wang, Dit-Yan Yeung, Wai-Kin Wong, and Wang-chun Woo. Convolutional lstm network: A machine learning approach for precipitation nowcasting. *arXiv preprint arXiv:1506.04214*, 2015.

[56] Hao Tang and James Glass. On training recurrent networks with truncated backpropagation through time in speech recognition. In *2018 IEEE Spoken Language Technology Workshop (SLT)*, pages 48–55. IEEE, 2018.

[57] Martín Abadi, Ashish Agarwal, Paul Barham, Eugene Brevdo, Zhifeng Chen, Craig Citro, Greg S. Corrado, Andy Davis, Jeffrey Dean, Matthieu Devin, Sanjay Ghemawat, Ian Goodfellow, Andrew Harp, Geoffrey Irving, Michael Isard, Yangqing Jia, Rafal Jozefowicz, Lukasz Kaiser, Manjunath Kudlur, Josh Levenberg, Dandelion Mané, Rajat Monga, Sherry Moore, Derek Murray, Chris Olah, Mike Schuster, Jonathon Shlens, Benoit Steiner, Ilya Sutskever, Kunal Talwar, Paul Tucker, Vincent Vanhoucke, Vijay Vasudevan, Fernanda Viégas, Oriol Vinyals, Pete Warden, Martin Wattenberg, Martin Wicke, Yuan Yu, and Xiaoqiang Zheng. TensorFlow: Large-scale machine learning on heterogeneous systems, 2015. Software available from tensorflow.org.

[58] Francois Chollet et al. Keras, 2015.

[59] Felix A Gers, Nicol N Schraudolph, and Jürgen Schmidhuber. Learning precise timing with lstm recurrent networks. *Journal of machine learning research*, 3(Aug):115–143, 2002.

[60] Sepp Hochreiter, Martin Heusel, and Klaus Obermayer. Fast model-based protein homology detection without alignment. *Bioinformatics*, 23(14):1728–1736, 2007.

[61] R Rodriguez and Isabel Gutiérrez. Unified formulation to predict the tensile curves of steels with different microstructures. In *Materials Science Forum*, volume 426, pages 4525–4530. Trans Tech Publications Ltd., Zurich-Uetikon, Switzerland, 2003.

[62] J Kadkhodapour, A Butz, S Ziaei-Rad, and S Schmauder. A micro mechanical study on failure initiation of dual phase steels under tension using single crystal plasticity model. *International Journal of Plasticity*, 27(7):1103–1125, 2011.

[63] T Maki. Morphology and substructure of martensite in steels. *Phase transformations in steels*, pages 34–58, 2012.

[64] Harry Bhadeshia and Robert Honeycombe. *Steels: microstructure and properties*. Butterworth-Heinemann, 2017.

[65] Jidong Kang, Yuriy Ososkov, J David Embury, and David S Wilkinson. Digital image correlation studies for microscopic strain distribution and damage in dual phase steels. *Scripta Materialia*, 56(11):999–1002, 2007.

[66] H Ghadbeigi, Christophe Pinna, and Steven Celotto. Failure mechanisms in dp600 steel: Initiation, evolution and fracture. *Materials Science and Engineering: A*, 588:420–431, 2013.